Accepted Manuscript

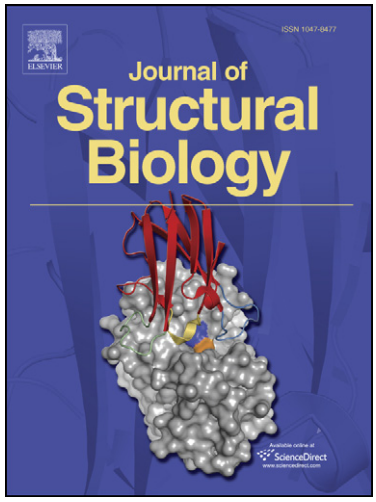

Characterization of biominerals in the radula teeth of the chiton, *Acanthopleura hirtosa*

Martin Saunders, Charlie Kong, Jeremy A. Shaw, David J. Macey, Peta L. Clode

PII: S1047-8477(09)00071-9
DOI: 10.1016/j.jsb.2009.03.003
Reference: YJSBI 5547

To appear in: *Journal of Structural Biology*

Received Date: 21 January 2009
Revised Date: 5 March 2009
Accepted Date: 6 March 2009

Please cite this article as: Saunders, M., Kong, C., Shaw, J.A., Macey, D.J., Clode, P.L., Characterization of biominerals in the radula teeth of the chiton, *Acanthopleura hirtosa*, *Journal of Structural Biology* (2009), doi: 10.1016/j.jsb.2009.03.003

Characterization of biominerals in the radula teeth of the chiton, *Acanthopleura hirtosa*

Martin Saunders[1], Charlie Kong[2], Jeremy A. Shaw[1], David J. Macey[3] and Peta L. Clode[1*]

[1] Centre for Microscopy, Characterisation and Analysis, The University of Western Australia, Crawley, WA 6009 Australia.

[2] Electron Microscopy Unit, University of New South Wales, Kingsford, NSW 2052 Australia.

[3] School of Biological Sciences & Biotechnology, Murdoch University, Murdoch, WA 6150 Australia.

Corresponding author:

Dr Peta L. Clode

CMCA (M010)

The University of Western Australia

Crawley, WA 6009 Australia

E-mail: peta.clode@uwa.edu.au

Phone: +61 8 6488 8098

Fax: +61 8 6488 1087

ABSTRACT:

Understanding biomineralization processes provides a route to the formation of novel biomimetic materials with potential applications in fields from medicine to materials engineering. The teeth of chitons (marine molluscs) represent an excellent example of a composite biomineralized structure, comprising variable layers of iron oxide, iron oxyhydroxide and apatite. Previous studies of fully mineralized teeth using X-ray diffraction, Raman spectroscopy and scanning electron microscopy (SEM) have hinted at the underlying microstructure, but have lacked the resolution to provide vital information on fine scale structure, particularly at interfaces. While transmission electron microscopy (TEM) is capable of providing this information, difficulties in producing suitable samples from the hard, complex biocomposite have hindered progress. To overcome this problem we have used focused ion beam (FIB) processing to prepare precisely oriented sections across interfaces in fully mineralized teeth. In particular, the composite structure is found to be more complex than previously reported, with additional phases (goethite and amorphous apatite) and interface detail observed. This combination of FIB processing and TEM analysis has enabled us to investigate the structural and compositional properties of this complex biocomposite at higher resolution than previously reported and has the potential to significantly enhance future studies of biomineralisation in these animals.

Key words: Biomineralization, chiton, magnetite, goethite, lepidocrocite, apatite, mollusc, TEM, FIB

INTRODUCTION:

The study of biomineralized structures can help to unravel the principles of hard tissue formation, such as teeth, shell or bone, and sits at the crossroads of bioinorganic and materials chemistry. It is a field that is key to the fabrication of novel biomimetic materials (Mann, 2001) and has the potential to contribute towards a broad range of applications in biology, medicine and materials science (Salata, 2004; Bar-Cohen, 2006). This broad potential is linked to the high level of structural complexity exhibited by biomineral forms, which are often organized in a hierarchical manner from the centimetre to the nano-scale (Weiner, 2008).

In chitons, which are marine molluscs, the teeth are composite structures comprised of both iron and calcium based biominerals. In a process that resembles a production line, each mineral phase is deposited sequentially in a step-wise fashion along the length of the radula, the ribbon-like feeding organ of the animal. In the chiton *Acanthopleura hirtosa*, magnetite is supported by an adjoining iron oxyhydroxide layer, previously reported to be lepidocrocite, which is, in turn, backed by calcium apatite, which fills the core of the tooth (Lee et al., 1998). With regard to our understanding of this complex biomineralization process, many questions remain unanswered. Of particular interest is how these composite biominerals are constructed with such precise spatial and temporal control, and how the different mineral phases interact to produce architecturally strong structures that resist crack propagation and breakage (van der Wal et al., 2000).

Early studies on the mature, mineralized teeth of chitons relied on bulk analyses, including X-ray diffraction of powdered preparations (Lowenstam, 1962; Towe and Lowenstam, 1967), and a combination of SEM imaging, energy-dispersive X-ray microanalysis and Raman spectroscopy (Lee et al., 2003), to investigate the mineral phases in the teeth.

This correlative approach provided useful elemental and mineralogical data on a gross scale, but was limited with respect to the resolution of fine detail. Such information can be obtained using TEM. However, TEM studies of biomineralized chiton teeth have to date been restricted to the very early stages of mineralization, where the preparation of suitably thin sections is relatively straightforward (Towe and Lowenstam, 1967; Kim et al., 1989). Our understanding of the latter stages of the biomineralization process has been inhibited by the difficulty of preparing suitable thin sections across the hard, mineralized layers in the fully mineralized composite material.

FIB techniques are routinely used to prepare cross- and thin-sections of hard materials for structural and elemental analysis in the physical sciences (Giannuzzi and Stevie, 2005; Mayer et al., 2007; Yao, 2007). However, there are only a small number of examples in the literature where these methods have been applied to biomineralization, including the study of mollusc sclerites (Suzuki et al., 2006) and shell (Valazquez-Castillo et al., 2006). FIB has also been applied to the study of interfaces between biological and innate surfaces in biomedical applications (Engqvist et al., 2006; Giannuzzi et al., 2007; Engqvist et al., 2008).

One reason for the limited number of FIB applications involving biomaterials is the possibility of sample damage occurring during preparation of the thin section, destroying the underlying microstructure. While this is true for soft biomaterials, potentially including the organic components in our samples, the hard composite mineral structure of chiton teeth is ideally suited to FIB processing. When applied to hard materials, FIB processing will create thin amorphous damage layers on the surfaces of the prepared sections, but the extent of surface amorphization and its impact on the underlying microstructure of the

material can be controlled, allowing detailed crystallographic and compositional information to be obtained in many cases (Mayer et al., 2007).

A significant benefit of FIB processing over conventional TEM preparation methods such as mechanical and ion polishing is the ability to control the specific location and orientation of the cross-section. This has allowed us to precisely target the interfaces between the various phases within chiton teeth, while ensuring that sections are prepared at the most suitable orientations to maximise the structural information obtainable. We have used this approach to obtain high quality, ultra-thin (<100nm) TEM sections across the mineral interfaces in chiton teeth. This has enabled us to investigate these interface regions in greater detail than has previously been possible, providing new insights into the microstructure of this complex biomineral.

MATERIALS AND METHODS:

Radula preparation:

Radulae were extracted from the chiton *Acanthopleura hirtosa* (Mollusca: Polyplacophora) that had been collected at Woodman Point, Perth, Australia. Soft tissues were removed and samples were resin embedded and polished in longitudinal section, as previously described (Shaw et al., 2008). Once polished, samples were carefully cut from the 1" embedding rings, mounted on stubs using double sided C tape and coated with 50nm of Au. Regions of interest (ROI) for FIB milling were initially identified from fully mineralized major lateral teeth using a SEM (Zeiss, 1555VP FESEM) operated at 15kV.

Preparation of thin sections:

A dual-beam FIB system (FEI Nova NanoLab 200) was used to prepare sections for TEM from fully mineralized major lateral teeth. Sections were acquired from the iron oxide - iron

oxyhydroxide interface, the iron oxyhydroxide - calcium apatite interface, and in some cases across both interfaces. ROI's were located and monitored within the dual-beam FIB using the electron beam imaging mode. The top surface of the ROI was protected with a strip of Pt (approximately 20μm x 2μm x 1μm) deposited in the FIB with a built-in gas injection source system. Material on both sides of the ROI was removed by an energetic Ga ion beam operating at 30kV with a beam current of 5nA. This produced a wedge-shaped slab of sample, approximately 18μm x 3μm x 5μm in size, in between the FIB troughs. The ion beam damaged layers on both sides of the slab that resulted from this initial high energy milling were subsequently removed by applying sequentially smaller beam currents, e.g. 1nA and 0.3nA, during a cleaning and thinning process. The resulting section, approximately 15μm x 3μm x 0.8μm, was cut free at one end and along the bottom with a 0.3nA ion beam at a tilt angle of 45°, leaving the section attached at one end only. The blade-shaped section with Pt protection layer on the top was then thinned to less than 100nm from both sides alternately, with a final ion beam current of 0.1nA. The redeposition of dust, generated during processing, on the surfaces of the final membrane was carefully cleaned with line scanning of the ion beam. The prepared section was then cut off from the fixed end, extracted under an optical microscope with an ex-situ micromanipulator system (Kleindiek), and mounted on a C-coated, formvar filmed Cu grid for TEM analysis.

Transmission electron microscopy:

All TEM imaging and diffraction was conducted at 120kV (JEOL, JEM-2100) using an 11Mpix CCD camera (Gatan, Orius1000). Care was taken to minimize the risk of beam damage by using the conventional approach of inserting an objective aperture located in the pole piece gap for imaging, and by spreading the beam to reduce intensity for selected area (SA) diffraction. Diffraction patterns were recorded with the digital camera, using

acquisition times of 5-10s per frame and averaging 5 frames to enhance the visibility of weak reflections. The majority of the data was obtained using the largest SA aperture, corresponding to a ~1μm field of view. Smaller apertures (the smallest giving a ~200nm field of view) were used to obtain localized information from interface features.

Electron energy-loss spectroscopy (EELS) was conducted on the same microscope using an energy-filter (Gatan, Tridiem). Spectra were obtained in imaging mode (diffraction coupling) using the spectrometer entrance aperture to select the required field of view. An energy dispersion of 0.3eV/pixel was used for all spectra and cumulative acquisition mode was used to obtain spectra with suitable signal-to-noise levels.

RESULTS:

General structure of FIB sections

The gross iron oxide, iron oxyhydroxide and calcium apatite mineral phases can be readily visualized in fully mineralized major lateral teeth in a SEM (Fig. 1). The iron oxide magnetite extends down the posterior face of the tooth, while the tooth core is comprised of calcium apatite. Between these two phases is an intermediate iron oxyhydroxide layer, previously identified as lepidocrocite (Lee et al., 1998). From these preparations, specific mineral phases and interfaces could be easily identified and selected with precision for FIB milling of thin sections (Fig. 2). The resulting FIB sections were highly stable when imaged using TEM and the individual mineral regions, phase interfaces and overall gross structure could be clearly discerned (Fig. 3).

Fine Structure & Crystallography

The three regions, i.e. magnetite, intermediate iron oxyhydroxide and apatite, show distinctly different crystalline microstructures. The magnetite phase consists of large, 100-

500nm, grains that have a variety of grain morphologies with many exhibiting an elongated, roughly rectangular shape (Fig. 4A). SA diffraction (Fig. 4B, Table 1) shows no strong crystallographic orientation relationship between neighbouring magnetite grains.

The apatite layer consists of small (<100nm) grains with no distinct morphology and random orientation (Fig. 5A), resulting in a diffraction pattern containing broken rings (Fig. 5B). The apatite structure (Table 1) is consistent with that reported by Fleet et al. (2004). SA diffraction from the intermediate iron oxyhydroxide layer shows that it consists of two different phases, with different crystal structures and grain morphologies. The majority of the intermediate iron oxyhydroxide layer, from the magnetite interface to close to the apatite interface, is comprised of randomly oriented grains 100-200nm in size (Fig. 6A). The diffraction data from this region (Fig. 6B, Table 1) proves this phase to be goethite (α-FeOOH) rather than the previously reported lepidocrocite (γ-FeOOH). However, at the apatite interface, a number of elongated, oriented grains are observed extending out into the apatite region (Fig. 7A). Diffraction confirms that this region is lepidocrocite with strong crystallographic texture, i.e. common orientation of the crystals. From the diffraction data, it appears that the long axis of the elongated crystals corresponds to the <101> direction, which is consistent with the properties of synthetic lepidocrocite crystals described by Cornell and Schwertmann (2006) (Fig. 7B, Table 1). The presence of these two phases within the intermediate iron oxyhydroxide layer is not initially apparent because goethite and lepidocrocite are two forms of the same iron oxyhydroxide phase. As such, there is no mass/density contrast visible between these two phases in conventional bright field TEM images or SEM back-scattered images and it is only from the diffraction data (Table 1) that the presence of both can be determined.

The interfaces between the different phases are not sharp, with significant interleaving between the adjoining phases at each of the interfaces. In addition to the extension of the lepidocrocite grains into the apatite region, isolated grains of goethite are found well into the neighbouring magnetite layer and vice versa (not shown). This cannot simply be attributed to the cutting angle of the section across the interface because the use of the dual-beam FIB allows accurate orientation of the cross-section with respect to the interface. Analysis of the intermediate iron oxyhydroxide - apatite boundary also indicates that an amorphous apatite phase is formed as a buffer between the crystalline apatite and lepidocrocite phases (Fig. 8A and 8B). This amorphous layer appears to be continuous along the boundary with a maximum thickness of ~200nm, making it possible to obtain data solely from this phase using the smallest SA aperture. It was observed in FIB sections taken from various interface locations within the same tooth. The composition of the layer was confirmed by EELS, with the spectrum obtained from the amorphous interface phase (Fig. 8C) matching that obtained from within the crystalline apatite region (Fig. 8D).

DISCUSSION:

The ability to prepare high quality, thin (<100nm) sections with precise control over the location and orientation from these biomineralized structures provides new and exciting opportunities for understanding the biological and chemical processes and interactions that design, co-ordinate and control mineral formation and growth in this system. By analyzing FIB sections prepared from fully mineralized chiton teeth, we have, for the first time, been able to characterize the fine crystal structure of each of the different mineral phases. From this we can obtain new insights into the microstructure and phase composition of the various mineralized layers (Fig. 9). Importantly, we have shown that the central iron oxyhydroxide layer is predominantly composed of goethite, with lepidocrocite only present at the calcium apatite edge. This is consistent with initial work done by

electron diffraction on early-mineralized teeth (Kim et al., 1989), but is inconsistent with more recent Raman data from fully mineralized teeth (Lee et al., 1998), which reported that this region was composed solely of lepidocrocite. However, given our new understanding of the substructure of the iron oxyhydroxide layer, it is evident that the limited spatial resolution (10-15μm) of the Raman technique would have meant that it would not have been possible to gain a true analysis of the goethite and lepidocrocite regions. Reappraisal of the original Raman data suggests that goethite peaks are present in Lee et al.'s Raman spectra, but was not recognized by the authors because of overlap between the characteristic peaks of goethite and lepidocrocite.

Another important discovery is the presence of an amorphous apatite layer at the lepidocrocite – apatite interface. While FIB processing is expected to induce a thin amorphous layer on the surface of the section, the formation of a purely amorphous phase through the entire thickness of the section and confined to a narrow band at the lepidocrocite - apatite interface cannot be easily explained as a FIB preparation artefact. This layer has not previously been observed, as suitable TEM samples could not be prepared from fully mineralized teeth. Given the significant difference in atomic planar spacings in the crystal structures of the two phases (see Table 1), the presence of this amorphous phase at the interface is not unexpected. Analysis of the diffraction data from the amorphous region shows that the maximum intensity in the first amorphous ring, corresponding to the most probable nearest neighbor atom spacing in the interface phase, is at ~0.31nm. This is the first spacing that is common to both the lepidocrocite and apatite structures and matches the {101} lepidocrocite spacing that repeats along the length of the lepidocrocite needles.

Close scrutiny of the grains in Figs. 4-7, reveals that, while the grain size appears be on the 100s of nm scale in all cases, there is some evidence of a grain substructure on smaller length scales. It is known that the precursor mineral phases in the immature teeth form at the 10s of nm scale (Kim et al., 1989). Thus, it is possible that this substructure in the mature teeth is a relic of the precursor mineral grains, which have coalesced to form the larger grains in the mature teeth. This mechanism of formation would be consistent with the concept of mesocrystals, where smaller sub-units combine in an ordered fashion to produce larger ordered structures (Cölfen and Antonietti, 2005). However, further work is required to compare the development of the mineral phases from the immature to mature end of the radula before strong conclusions can be made in this regard.

By making use of FIB processing we have been able to produce precisely oriented sections across specific mineral boundaries, allowing us to investigate the nature of the interfaces between different mineral phases. Expanding on earlier work, which demonstrated that on the gross scale each mineral region was not a discreet compartment, but overlapped adjacent phases (Wealthall et al., 2005), we can now demonstrate that interface regions have very complex fine scale microstructures where individual crystals of different phases intersect quite significantly.

With regard to biomimetics and the fabrication of materials, a key aspect is the interaction between the different mineral phases and the means by which the composite layered structure is used to produce the strength, integrity and functionality of the overall biomineralized structure. Curiously, when manually placed under strain, chiton teeth do not fracture along the mineral interfaces (Wealthall et al., 2005), suggesting a strong bond between very different materials. It is immediately apparent from the FIB sections that individual layers lock together by the intergrowth of one phase into its neighbour. The

discovery that the fully-mineralized teeth contain a composite goethite/lepidocrocite layer rather than the previously reported simple lepidocrocite layer and the formation of an amorphous apatite layer where it connects to the iron oxide phase is further evidence that these biomineralized structures are more complex than previously considered.

While further work is required to fully understand the complicated microstructure revealed in these FIB sections, it is apparent that the use of FIB methods to prepare thin sections across the various layers in fully mineralized chiton teeth has allowed us to redefine the fine scale crystal structure of these complex biominerals and has opened up new opportunities to study these materials at a previously unconsidered scale. Without fundamental information regarding mineral phases, their distribution within the material, and their association with each other, our understanding of biomineralization processes will remain limited.

Acknowledgements: The authors acknowledge the facilities, scientific and technical assistance of the Australian Microscopy & Microanalysis Research Facility at both the Centre for Microscopy, Characterisation & Analysis, UWA and the Electron Microscopy Centre, UNSW, facilities funded by the Universities, State and Commonwealth Governments. Financial support was provided by an ARC Discovery Grant (DP0559858) and a NANO TAP grant.

REFERENCES:

Bar-Cohen, Y., 2006. Biomimetics: Biologically Inspired Technologies CRC Press, Boca Raton.

Cölfen, H., and M. Antonietti, 2005. Mesocrystals: inorganic superstructures made by highly parallel crystallization and controlled alignment. Angewandte Chemie International Edition 44: 5576-5591.

Cornell, R.M., and U. Schwertmann, 2006. The iron oxides: structure, properties, reactions, occurrences and uses. 2nd Ed. Wiley-VCH, Weinheim.

Engqvist, H., F. Svahn, T. Jarmar, R. Detsch, H. Mayr, P. Thomsen, and G. Ziegler, 2008. A novel method for producing electron transparent films of interfaces between cells and biomaterials. Journal of Materials Science-Materials in Medicine 19: 467-470.

Engqvist, H., G.A. Botton, M. Couillard, S. Mohammadi, J. Malmstrom, L. Emanuelsson, L. Hermansson, M.W. Phaneuf, and P. Thomsen, 2006. A novel tool for high-resolution transmission electron microscopy of intact interfaces between bone and metallic implants. Journal of Biomedical Materials Research Part A 78A: 20-24.

Fleet, M.E., X. Liu, and P.L. King, 2004. Accommodation of the carbonate ion in apatite: An FTIR and X-ray structure of crystals synthesized at 2-4GPa. American Mineralogist 89: 1422-1432.

Giannuzzi, L.A., and F.A. Stevie, 2005. Introduction to Focused Ion Beams: Instrumentation, Theory, Techniques, and Practice. Springer.

Giannuzzi, L.A., D. Phifer, N.J. Giannuzzi, and M.J. Capuano, 2007. Two-dimensional and 3-dimensional analysis of bone/dental implant interfaces with the use of focused ion beam and electron microscopy. Journal of Oral and Maxillofacial Surgery 65: 737-747.

Kim, K.S., D.J. Macey, J. Webb, and S. Mann, 1989. Iron mineralisation in the radula teeth of the chiton *Acanthopleura hirtosa*. Proceedings of the Royal Society London B 237: 335-346.

Lee, A.P., L.R. Brooker, W. Van Bronswijk, D.J. Macey, and J. Webb, 2003. Contribution of Raman spectroscopy to identification of biominerals present in teeth of *Acanthopleura rehderi, Acanthopleura curtisiana,* and *Onithochiton quercinus*. Biopolymers 72: 299-301.

Lee, A.P., J. Webb, D.J. Macey, W. van Bronswijk, A.R. Savarese, and G.C. de Witt, 1998. *In situ* Raman spectroscopic studies of the teeth of the chiton *Acanthopleura hirtosa*. Journal of Biological Inorganic Chemistry 3: 614-619.

Lowenstam, H.A., 1962. Magnetite in denticle capping in recent chitons (Polyplacophora). Geological Society of America Bulletin 73: 435-438.

Mann, S., 2001. Biomineralization, Principals and Concepts in Bioinorganic Materials. Chemistry Oxford University Press, Oxford.

Mayer, J., L.A. Giannuzzi, T. Kamino, and J. Michael, 2007. TEM Sample preparation and FIB-induced damage. MRS Bulletin 32: 400-407.

Salata, O.V., 2004. Applications of nanoparticles in biology and medicine. Journal of Nanobiotechnology 2: 3.

Shaw, J.A., D.J. Macey, P.L. Clode, L.R. Brooker, R.I. Webb, E. Stockdale, and R.M. Binks, 2008. Methods of sample preparation of epithelial tissue in chitons (Mollusca: Polyplacophora). American Malacological Bulletin 25: 35-41.

Suzuki, Y., R.E. Kopp, T. Kogure, A. Suga, K. Takai, S. Tsuchida, N. Ozaki, K. Endo, J. Hashimoto, Y. Kato, C. Mizota, T. Hirata, H. Chiba, K.H. Nealson, K. Horikoshi, and J.L. Kirschvink, 2006. Sclerite formation in the hydrothermal-vent "scaly-foot" gastropod--possible control of iron sulfide biomineralization by the animal. Earth and Planetary Science Letters 242: 39-50.

Towe, K.M., and H.A. Lowenstam, 1967. Ultrastructure and development of iron mineralization in the radular teeth of *Cryptochiton stelleri* (Mollusca). Journal of Ultrastructure Research 17: 1-13.

Valazquez-Castillo, R., J. Reyes-Gasga, D.I. Garcia-Gutierrez, and M. Jose-Yacaman, 2006. Nanoscale characterization of nautilus shell structure: an example of natural self-assembly. Journal of Materials Research 21: 1484-1489.

van der Wal, P., H.J. Giesen, and J.J. Videler, 2000. Radular teeth as models for the improvement of industrial cutting devices. Materials Science & Engineering C-Biomimetic and Supramolecular Systems 7: 129-142.

Wealthall, R.J., L.R. Brooker, D.J. Macey, and B.J. Griffin, 2005. Fine structure of the mineralized teeth of the chiton *Acanthopleura echinata* (Mollusca: Polyplacophora). Journal of Morphology 265: 165-175.

Weiner, S., 2008. Biomineralization: A structural perspective. Journal of Structural Biology 163: 229-234.

Yao, N., 2007. Focused Ion Beam Systems: Basics and Applications. Cambridge University Press.

FIGURE LEGENDS:

FIG. 1: Back-scattered SEM micrograph displaying the gross distribution of mineral phases within two fully mineralized, major lateral teeth. The iron oxide magnetite (M) extends along the posterior face of the tooth, while calcium apatite (Ca) fills the core. Between these two regions is the intermediate iron oxyhydroxide region (I). Scale = 50μm.

FIG. 2: SEM micrograph showing example locations of FIB milling, with resulting TEM sections (arrows) sitting in the milled trough prior to extraction. The magnetite (M), intermediate iron oxyhydroxide (I) and calcium apatite (Ca) regions of the tooth are easily visualized for precise FIB milling. Section 1 (*i*) crosses the magnetite – intermediate iron oxyhydroxide interface, while section 2 (*ii*) crosses the intermediate iron oxyhydroxide – calcium apatite interface. Scale = 20μm.

FIG. 3: Low magnification TEM micrograph of a typical FIB section showing magnetite (M), intermediate iron oxyhydroxide (I) and calcium apatite (Ca) phases and interfaces (arrows). The protective platinum layer (p) is also visible. Scale = 1μm.

FIG. 4: (A) TEM micrograph of the magnetite region showing the large angular grains. Scale = 300nm. (B) Corresponding SA diffraction pattern. The coloured rings correspond to the six planar spacings identified in Table 1.

FIG. 5: (A) TEM micrograph of the apatite region showing the small (<100nm), non-uniform grains. Scale = 200nm. (B) Corresponding SA diffraction pattern. The coloured rings correspond to the six planar spacings identified in Table 1.

FIG. 6: (A) TEM micrograph of the goethite region showing the 100-200nm grains. Scale = 100nm. (B) Corresponding SA diffraction pattern. The coloured rings correspond to the six planar spacings identified in Table 1.

FIG. 7: Interface of intermediate iron oxyhydroxide (I) and calcium apatite (Ca) phases. (A) TEM micrograph of the lepidocrocite – apatite interface showing elongated, ordered lepidocrocite grains. Scale = 300nm. (B) SA diffraction pattern from area marked with a circle in A, showing texture of lepidocrocite grains. The arrows identify the {101} reflection, which is aligned along the long axis of the elongated grains (consistent with the orientation of synthetic lepidocrocite grains reported by Cornell and Schwertmann (2006)).

FIG. 8: Interface of intermediate iron oxyhydroxide (I) and calcium apatite (Ca) phases. (A) TEM micrograph of lepidocrocite – apatite interface. Scale = 300nm. (B) SA diffraction pattern from area marked with circle in C confirming presence of amorphous phase at interface. The semi-circle marks the maximum intensity in the first amorphous ring at a spacing of ~0.31nm. (C) EELS spectrum obtained from the amorphous phase confirming the presence of Ca, P and O. (D) EELS spectrum obtained from the crystalline apatite phase, which matches that shown in C. The carbon peak in both spectra is a combination of the organic component of the sample and the carbon support film.

FIG. 9: Schematic diagram to show the revised structure of fully mineralized teeth in the chiton, *Acanthopleura hirtosa*, as determined from FIB-prepared sections and TEM imaging and diffraction analysis. Magnetite (M), goethite (G), lepidocrocite (L), amorphous calcium apatite (ACa) and crystalline calcium apatite (CCa) regions are depicted.

Table 1: Published planar spacing values for magnetite, goethite, lepidocrocite and calcium apatite compared to experimental values obtained from the selected area diffraction (SAD) patterns shown in Figures 4-7.

Magnetite		SAD	**Goethite**		SAD	**Lepidocrocite**		SAD	**Apatite**		SAD
hkl	d (nm)	data	hkl	d (nm)	data	hkl	d (nm)	data	hkl	d (nm)	data
111	0.485	0.49	200	0.498	0.51	200	0.627	0.62	100	0.817	0.82
220	0.297	0.30	101	0.418	0.43	210	0.329	0.33	101	0.526	0.53
311	0.253	0.26	201	0.338	0.35	101	0.298	0.31	110	0.472	0.48
222	0.242	0.22	301	0.269	0.28	301	0.247	0.25	200	0.409	0.41
422	0.171	0.17	210	0.258	0.26	410	0.243	0.23	111	0.389	0.40
511	0.162	0.16	011	0.253	0.25	600	0.207	0.21	201	0.351	0.35

Published planar spacings obtained from Cornell and Schwertmann (2006) and Fleet et al (2004).

Figure 1, 2 and 3

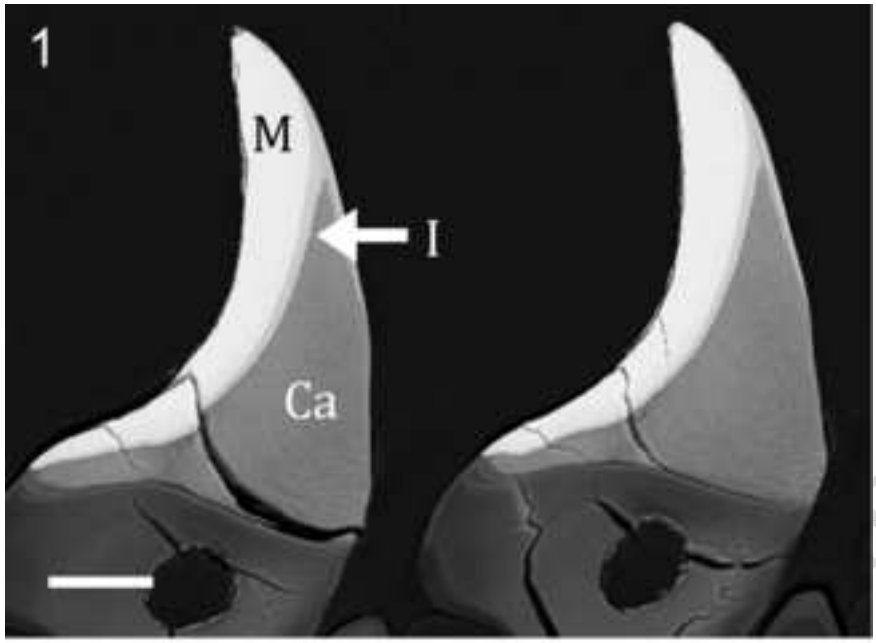

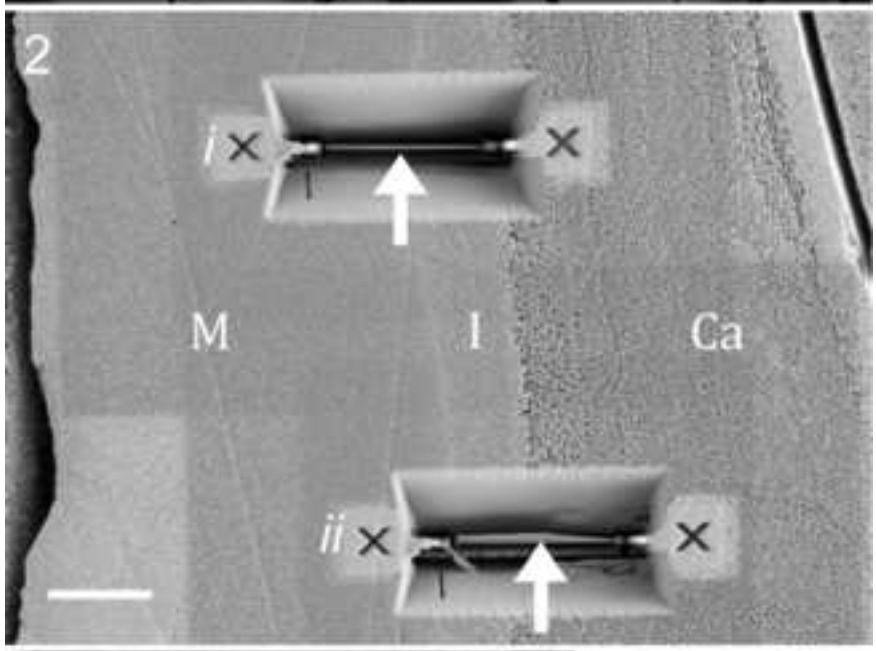

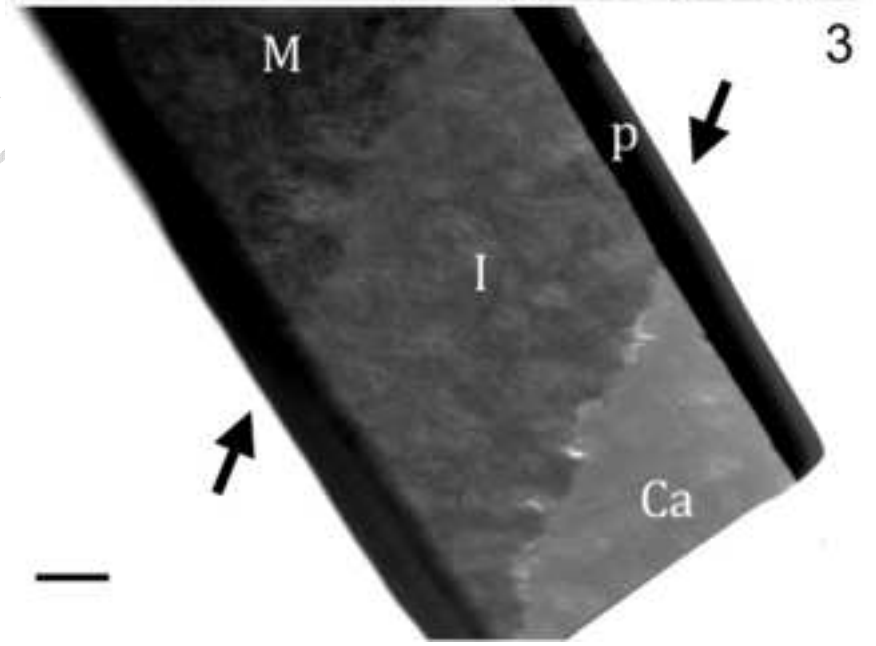

Figure 4

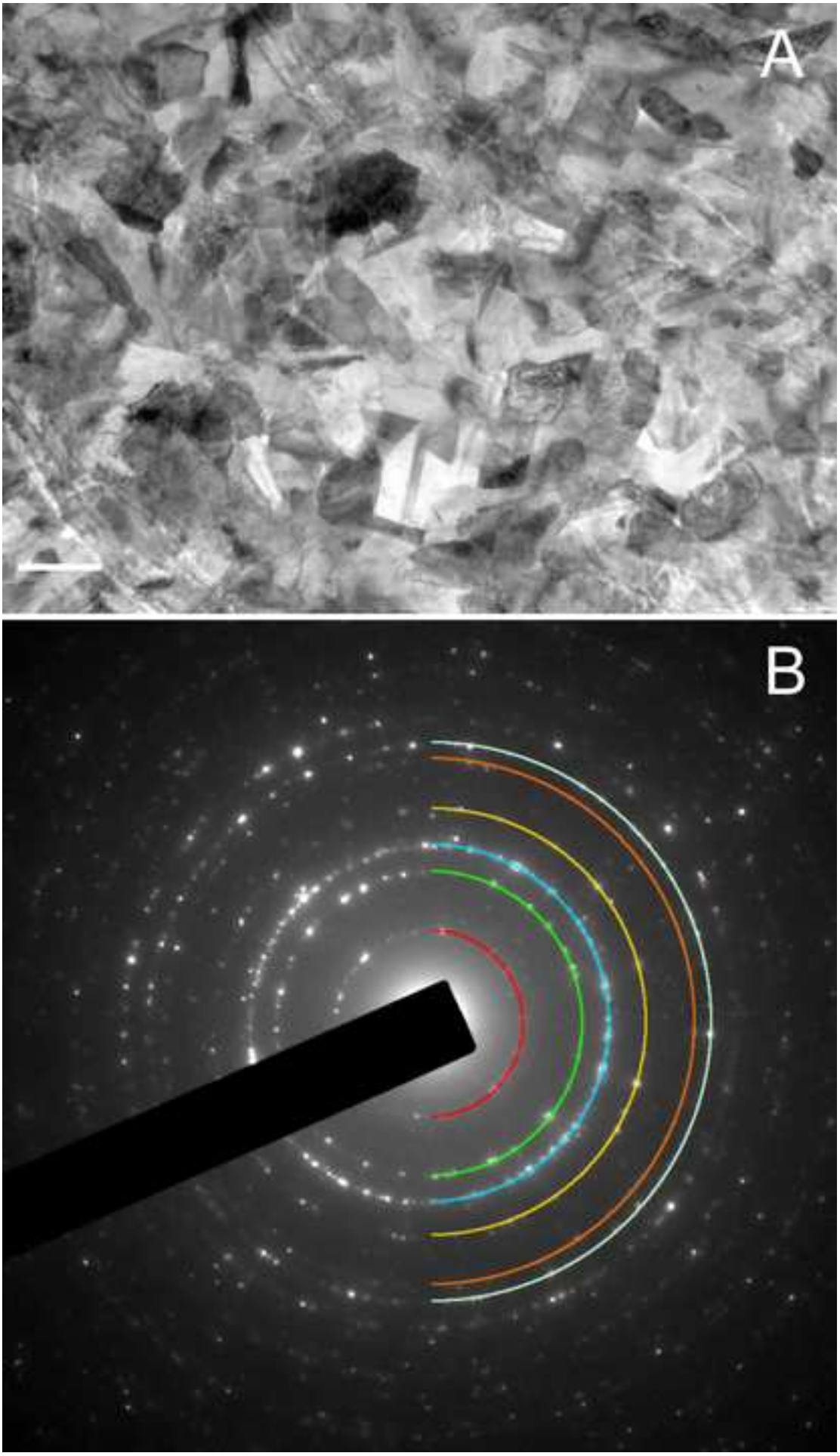

Figure 5

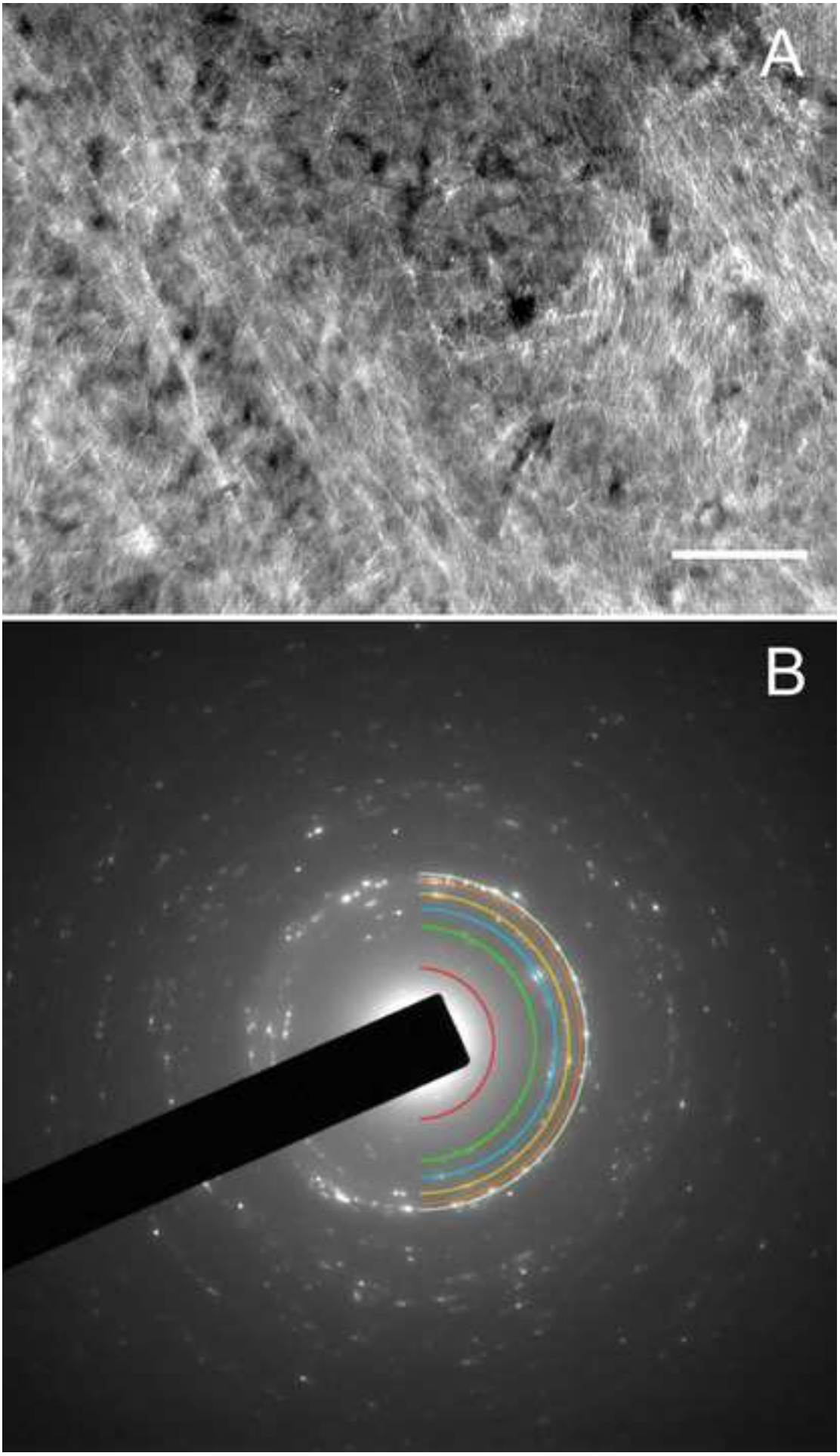

Figure 6

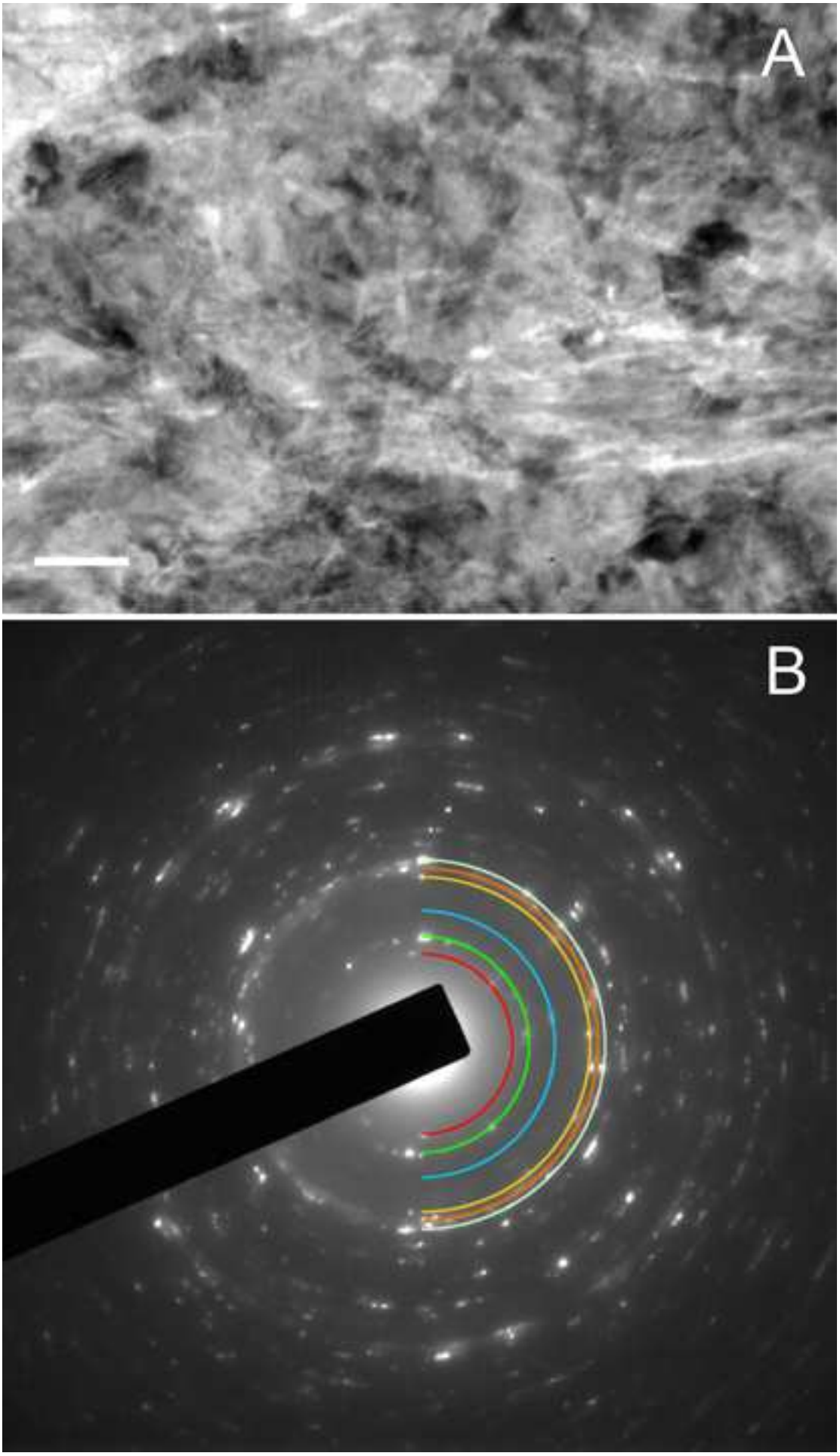

Figure 7

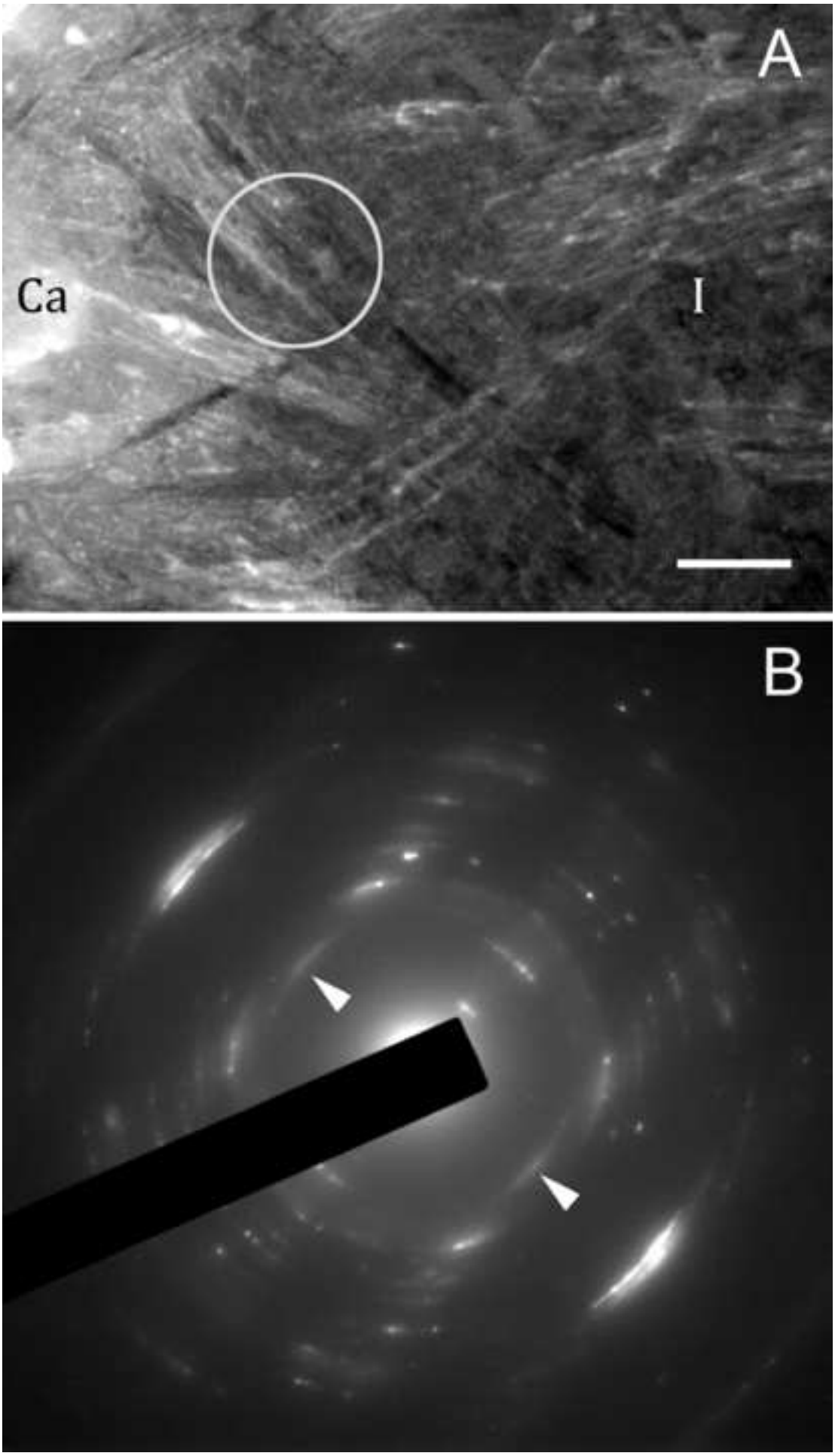

Figure 8

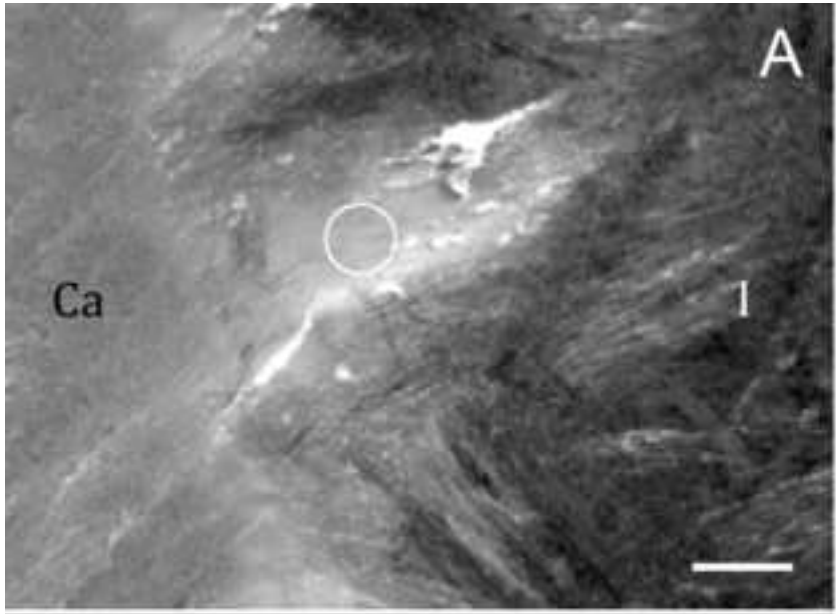
A
Ca
I

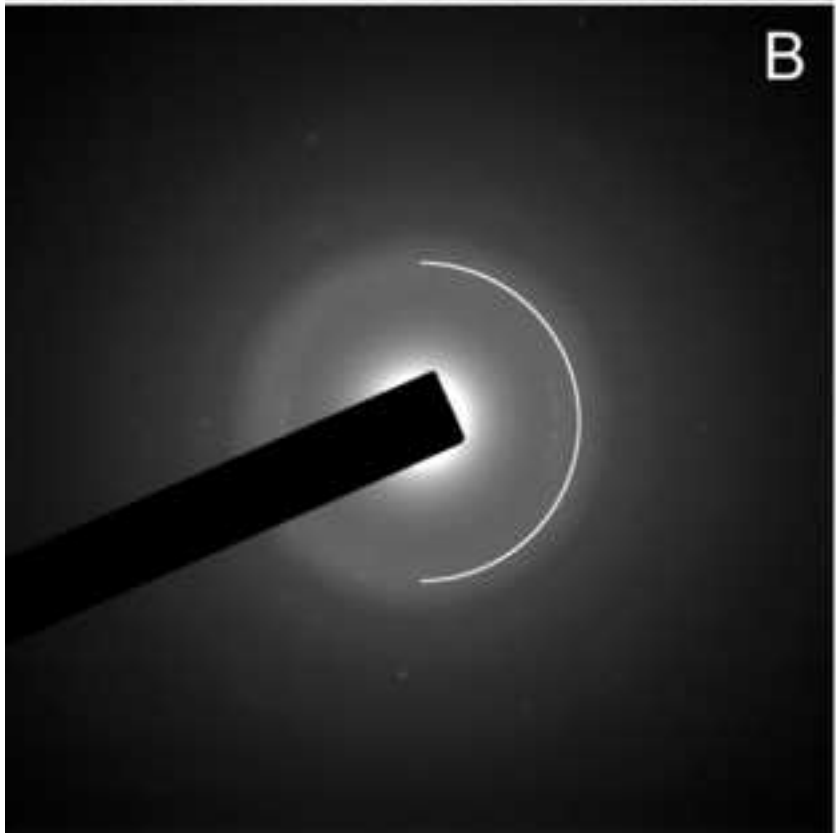
B

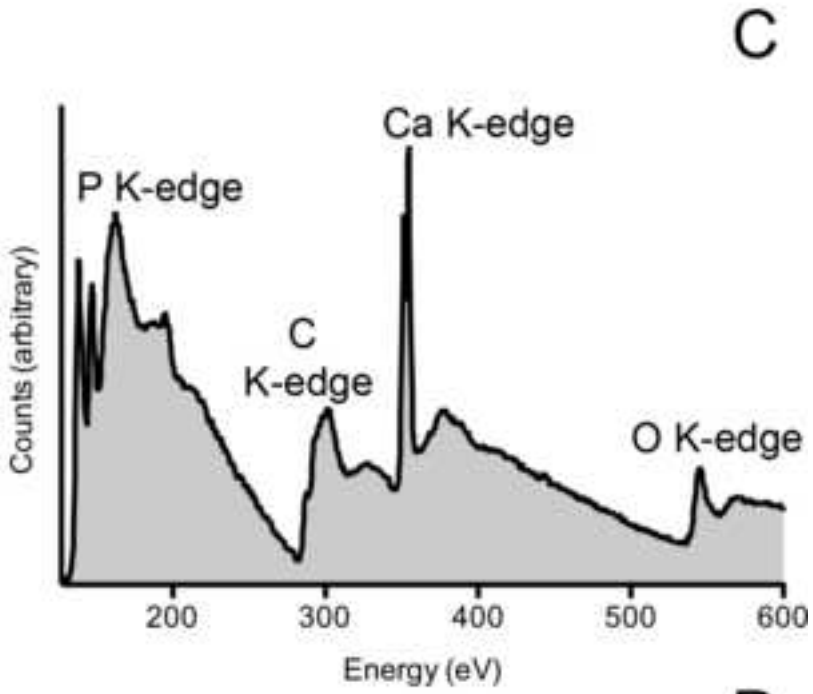
C
Ca K-edge
P K-edge
C
K-edge
O K-edge
Counts (arbitrary)
200
300
400
500
600
Energy (eV)

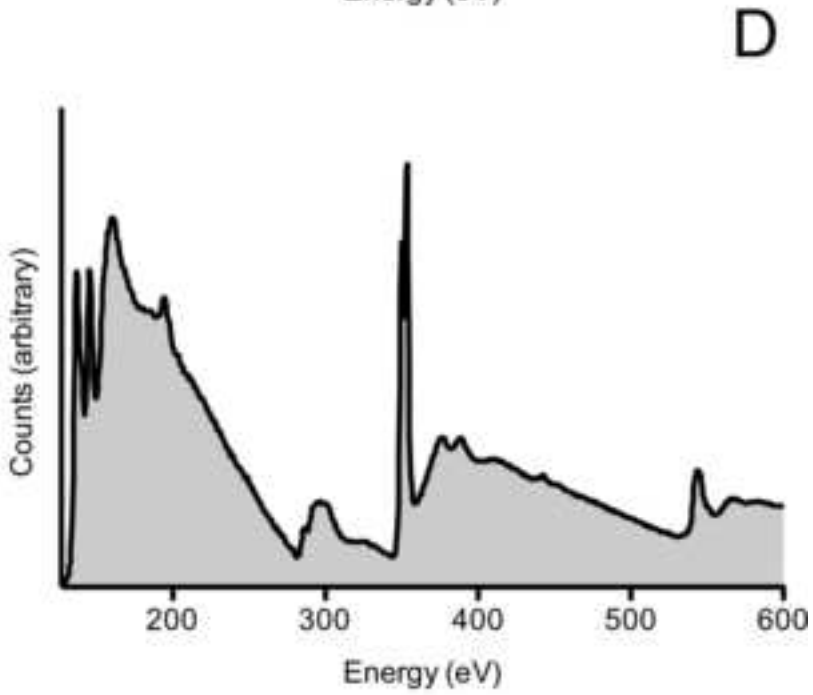
D
Counts (arbitrary)
200
300
400
500
600
Energy (eV)

Figure 9